CHALMERS
UNIVERSITY OF TECHNOLOGY

Microstructure, mechanical properties and fracture mechanisms in a 7017 aluminium alloy tailored for powder bed fusion – laser beam

Materials & Design 226 (2023) 111602

Contents lists available at ScienceDirect

Materials & Design

journal homepage: www.elsevier.com/locate/matdes

Microstructure, mechanical properties and fracture mechanisms in a 7017 aluminium alloy tailored for powder bed fusion – laser beam

Bharat Mehta [a,*], Tatiana Mishurova [b], Sergei Evsevleev [b], Henning Markötter [b], Giovanni Bruno [b], Eduard Hryha [a], Lars Nyborg [a], Eero Virtanen [c]

[a] Department of Industrial and Materials Science, Chalmers University of Technology, Gothenburg, Sweden
[b] Bundesanstalt für Materialforschung und -Prüfung (BAM), Unter den Eichen 87, 12205 Berlin, Germany
[c] EOS Electro Optical Systems Finland Oy, Turku, Finland

HIGHLIGHTS

- 7017 Al alloy admixed with 3 wt% Zr, 0.5 wt% TiC created fully dense samples (<0.2 % porosity) processed via PBF-LB process.
- Microstructure shows strengthening as a combination of precipitation hardening and grain size strengthening.
- In-situ combined with ex-situ tensile testing confirm Zr inclusions improve ductility by deflecting crack growth.

GRAPHICAL ABSTRACT

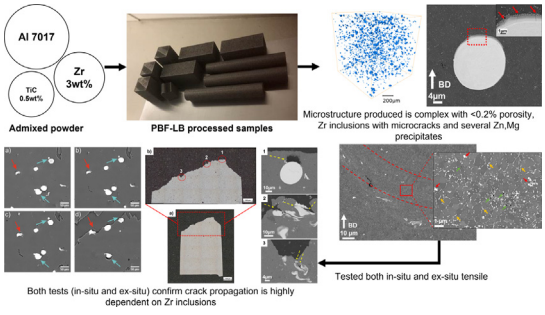

ARTICLE INFO

Article history:
Received 31 August 2022
Revised 15 December 2022
Accepted 5 January 2023
Available online 07 January 2023

Keywords:
Additive manufacturing
Powder bed fusion – Laser beam
Strengthening mechanisms
X-ray computed tomography
Crack propagation
Zirconium

ABSTRACT

This study addressed a 7017 Al-alloy tailored for powder bed fusion – laser beam (PBF-LB) process. The alloy was prepared by mixing 3 wt% Zr and 0.5 wt% TiC powder to standard pre-alloyed 7017 grade aluminium powder. This made printing of the alloys possible avoiding solidification cracking in the bulk and achieving high relative density (99.8 %). Such advanced alloys have significantly higher Young's modulus (>80 GPa) than conventional Al-alloys (70–75 GPa), thus making them attractive for applications requiring high stiffness. The resulting microstructure in as-printed condition was rich in particles originating from admixed powders and primary precipitates/inclusions originating from the PBF-LB process. After performing a T6-like heat treatment designed for the PBF-LB process, the microstructure changed: Zr-nanoparticles and Fe- or Mg/Zn- containing precipitates formed thus providing 75 % increase in yield strength (from 254 MPa to 444 MPa) at the cost of decreasing ductility (~20 % to ~9 %). In-situ tensile testing combined with SXCT, and ex-situ tensile testing combined with fracture analysis confirmed that the fracture initiation in both conditions is highly dependent on defects originated during printing. However, cracks are deflected from decohesion around Zr-containing inclusions/precipitates embedded in the Al-matrix. This deflection is seen to improve the ductility of the material.

1. Introduction

A combination of high electrical and thermal conductivity, general corrosion resistance and high specific strength makes aluminium alloys lucrative for applications demanding lightweighting combined with secondary needs [1]. Additive manufac-

* Corresponding author.

https://doi.org/10.1016/j.matdes.2023.111602
0264-1275/

turing (AM) [2] enables a layer-by-layer fabrication of complex geometries thereby enabling improved product designs. Combined with improved product design, the processing conditions during AM, particularly powder bed fusion – laser beam (PBF-LB) such as high cooling rates of 10^3-10^5 K/s [2,3] enable alloy designers to tailor novel compositions of alloys. When it comes to aluminium alloys designed for PBF-LB process, the major concern with printability is related to solidification cracking which is prevalent in 2xxx, 6xxx and 7xxx series aluminium alloys [4–6]. Such cracking has shown to be detrimental as it spans across several layers of a printed sample, thus, rendering the printed material useless for load bearing applications. One way to avoid solidification cracking is the addition of extra alloying elements or materials, such as Zr, TiB_2, via ex-situ mixing [7] or in-situ alloying [8,9]. This helps to provide sites for heterogeneous nucleation thus reducing stresses at grain boundaries and providing crack free aluminium alloys with isotropic properties. A second method utilized by alloy designers is to develop entirely new alloy recipes [10,11] which provide alloy systems inherently resistant to solidification cracking. Most of the alloy designers have focused on high strength as the most relevant property [6,12,13]. Although it is reasonable to select strength as a factor, the secondary properties make aluminium appealing for most applications. For example, Cann et al. [14] have suggested that the improvement of the load bearing capacity of aluminium above operating temperatures of 493 K could be significantly beneficial for electrical cables and brazed heat-exchangers or heat-sinks. Following this idea, some researchers [9,10,15] have applied the principle of utilizing transition-series elements such as Mn, Ce or Zr as alloying elements combined with higher solubility enabled via PBF-LB. These studies have shown that thanks to the formation of precipitates at higher temperatures, such systems are resistant to strength loss up to 573 K or higher. Another application for high performance alloys could be components with stiffness-limited designs, such as aircraft wing spars, which need to resist bending deformation [16]. It is highly beneficial for an aluminium alloy to have higher Young's modulus to avoid such bending deformation while retaining high strength. Thus, it is important to leverage the alloy design tools available together with the knowledge of PBF-LB process to get the largest benefit to application-based alloys.

X-ray computed tomography (XCT) has been proven to be the best tool when estimating the effect of defects on mechanical properties of PBF-LB materials [17]. In case of complex microstructure containing additional phases (such as in case of alloying or admixed powder), XCT gives possibility to capture the spatial and size distribution of phases in 3D [18]. XCT, however, is naturally limited by its resolution and for the comprehensive investigation of the new materials at all scales should be often complemented by microscopy. Combining XCT acquisitions with a relevant loading scenario (in-situ testing) helps to give insight of the failure mechanism and damage behaviour of the material [19,20]. Such insights could be used not only for general description of damage in a material but for modelling or calibration of the mechanical experiment [21].

This study presents a novel 7017 aluminium alloy based on a pre-alloyed base composition of 7017 alloy in powder form with ex-situ addition of 3 wt% Zr and 0.5 wt% TiC. This ex-situ addition made the alloy printable while providing a significantly higher stiffness (~15–20 % increase) compared to conventional Al-alloys and possesses high yield strength of ~ 445 MPa in heat treated condition. The study focuses on as-printed, and heat treated microstructure with help of powerful characterization tools such as electron microscopy and synchrotron X-ray computed tomography (SXCT). To understand the damage mechanism tensile tests were carried out both in-situ combined with SXCT, and ex-situ followed by fracture section analysis. This methodology is successful for lighter alloys such as Al due to good atomic contrast between Al-matrix and precipitates (especially Zr). This approach also helps to investigate the cause of fractures and suggest possible mitigation techniques for improvement of the mechanical behaviour.

2. Materials and methods

2.1. Materials

The source material was prepared by taking a 7017 Aluminium alloy powder (20–63 μm standard size) and combining it with 3 wt % elemental Zr powder and 0.5 wt% TiC powder. Powder particle size distribution was measured with laser diffraction analyser Microtrack S3500 wet method according to ASTM B822-17. The three powders were combined by a process of dry mixing. The final composition was measured with ICP-OES process according to ASTM E3061-17 as shown in Table 1.

2.2. Manufacturing and heat treatment of samples

All the printed samples were manufactured at EOS Finland Oy, Turku, Finland using a regular EOS M290 machine equipped with a 100 μm spot size and 400 W (370 W nominal) power Yb-fiber laser. The samples were fabricated with standard processing parameters utilizing a volumetric energy density of 60 J/mm^3 consisting of 40 μm layer thickness and infill with 7 mm stripes. Platform preheating temperature was 195 °C (468 K) and argon processing gas was used with residual oxygen content below 0.1 % in process chamber. Standard HSS recoater blade and EOS M290 standard inlet nozzle were used. The mentioned parameter set was considered to produce fully dense samples (>99.5 % density). The samples were printed as 20 mm side cubes, and then cut into pieces to perform microscopy analysis along different directions (build and transverse to build direction), as shown in Fig. 1a. For in-situ tensile testing, prisms of 50 mm × 20 mm × 20 mm were printed horizontally (long edge in the layer plane), and then the tensile samples were machined by electro discharge machining (EDM) as shown in Fig. 2. For ex-situ tensile testing, cylindrical samples of 95 mm length and 14 mm diameter were printed horizontally in the same build job and machined to tensile bars according to ASTM E8 standard. The supplementary data section provides more information about the sample orientation and location on build plate. The samples were studied in as-printed (AP) and in heat treated (HT) conditions. The solution heat treatment was conducted in a Nabertherm NA 250/65 convection furnace with a ± 2 K temperature control at 713 K for 1 h. The samples were placed in a preheated furnace in order to minimize heating ramp-up which in this case is below 5 min. After solution heat treatment, all the samples were quenched in room-temperature (294 ± 3 K) water within 30 s from opening furnace door, followed by direct ageing at 393 K for 24 h in the mentioned convection furnace. In both cases K-type secondary thermocouples (with thin aluminium cover to avoid direct contact with the parts) were in contact with the parts during heat treatment to ensure temperature accuracy of ± 2 K.

2.3. Microstructural evaluation and analysis

The samples were cut along two directions (parallel and perpendicular to the build direction) followed by mounting on Polyfast conductive resin (from Struers). This was followed by grinding and polishing with 200, 500, 800, 2000 and 4000 grit silica foils followed by polishing with 1 μm diamond-based polish [10]. The final polishing step used was OP-S silica suspension. All samples were prepared on a Struers TegraPol 31 machine. The electron

Table 1
Composition of 7017 Aluminium alloy used, measured by ICP-OES. All contents in wt%. Content of other metallic elements was measured to be < 0.05 % each and 0.25 % total.

Al	Zn	Mg	Si	Fe	Mn	Cu	Zr	Ti
Bal.	4.4	2.3	0.45	0.4	0.23	0.01	3.1	0.49

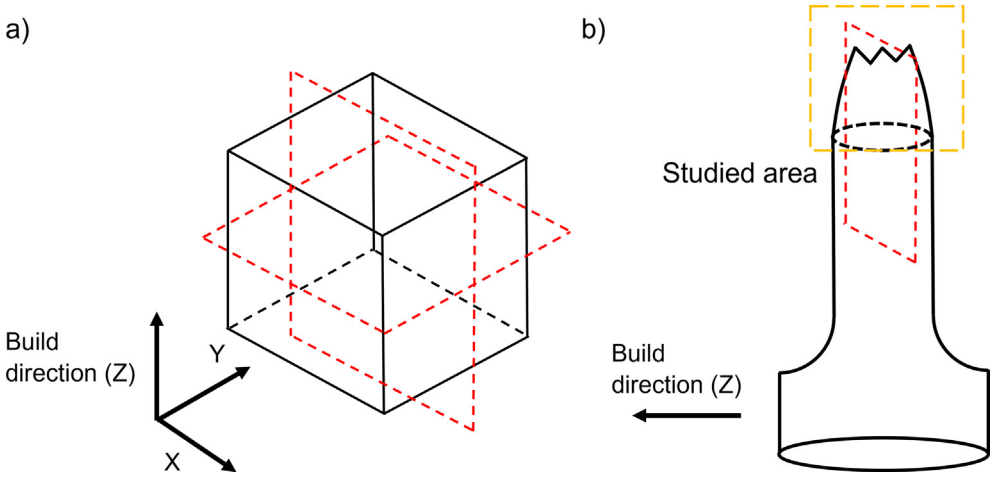

Fig. 1. A) Cubical samples used for microscopy analysis where the cutting planes are shown in red b) illustration of one side of ex-situ tensile sample (after testing). the cutting plane is shown in red and the sample as large as the orange area was tested from both sides of the cutting plane. the build direction for both the samples is shown. (For interpretation of the references to colour in this figure legend, the reader is referred to the web version of this article.)

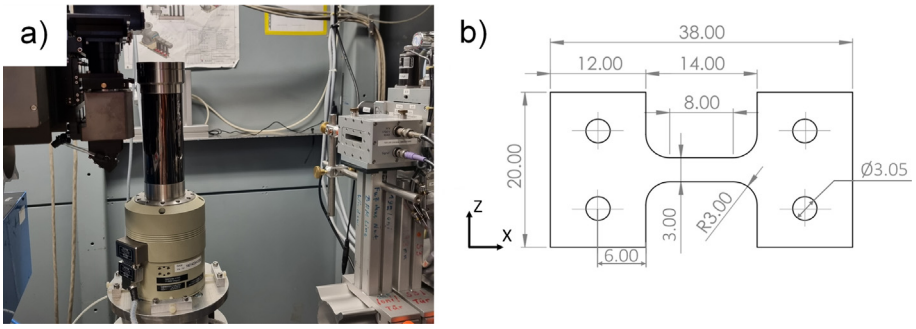

Fig. 2. A) Photograph of the in-situ tensile test set-up at the BAMline, b) drawing of the sample used in the in-situ tensile experiment. Note: the dimensions are in mm and the thickness is 3 mm. Z axis is aligned with the building direction.

microscopy was done using a Zeiss Gemini SEM 450 scanning electron microscope (SEM) with a field emission gun. The SEM was equipped with Bruker Quantax FlatQuad Energy Dispersive X-ray Spectroscopy (EDS) detector, which enabled chemical analysis at sub-micron resolutions using 4 kV operating voltage and 1nA of current.

2.4. Tensile testing and fractography

Tensile testing was conducted in an Instron 8501 servo-hydraulic testing machine equipped with fast electronic control system and 1 kHz data logging system. The test was conducted as per ASTM E8 standard with a strain rate of 0.01 % s^{-1}, and the strain was measured with an extensometer during the tests. For fractography section analysis, samples after tensile testing were cut into half close to the area of failure and cut section samples were mounted and grinded/polished in a similar method followed for microstructural evaluation. An illustration of sample geometry is shown in Fig. 1b.

2.5. Synchrotron X-ray computed tomography

The SXCT was conducted at the BAMline, BESSY II (Berlin, Germany), which is described in detail elsewhere [22,23]. At BAMline two scan modes are available, a step scan mode and a on-the-fly scan mode. In a step scan the rotation stage stops during the exposure of a projection, whereas in an on-the-fly scan the stage continuously rotates while the camera constantly takes projection images during the rotation. On-the fly scans offer a drastic reduction of scan times while step scans offer flexibility in scanning schemes that are optimised to reduce ring artefacts or to offer a preview reconstruction already during the scan.

The AP sample was machined to a cuboid with cross-section dimension of 1.1 × 1.1 mm^2. The ex-situ sample was scanned in step scan mode to improve data quality to the expense of scan time. The energy of the monochromatic X-ray beam was set to 30 keV, and an effective pixel size of 0.44 µm was achieved using a CCD camera with 10x objective. For the measurements the interlaced XCT acquisition protocol was used with 3232 projections, each with a counting time of 2.4 s. The reconstruction of 3D vol-

umes from 2D projections was made by BAM in-house developed software based on tomopy [24,25].

The in-situ tensile tests combined with SXCT were also conducted on the BAMline with DEBEN 5kN load rig installed on the rotation table (Fig. 2a). The samples with and without heat treatment were machined to the flat dog-bone sample geometry (see Fig. 2b). Prior to the experiment ex-situ tensile tests were performed. A pixel size of 1.44 μm was chosen, giving a field-of-view of about 3.6 mm. In this experiment, the energy of the monochromatic X-ray beam was set to 40 keV. On-the-fly XCT was performed with 2000 projections, each acquired with an exposure time of 0.5 s. The tensile test was conducted in load control mode in the elastic regime, and in displacement control in the plastic regime. The SXCT scan (of around 15 mins) was conducted after the nominal load was reached and stress relaxation ended.

For the SXCT data processing (aimed on the segmentation of different phases) reconstructed volumes were filtered by non-local means filter in Fiji ImageJ. The segmentation was performed using open source ilastik software [24], applying machine learning approach (based on the manual segmentation for the training datasets). This approach allows avoiding false segmentation of the ring artefacts and segment more precisely the different phases of multiphase materials. The distribution and volume fraction of different phases were analysed and visualized in Avizo software [26].

3. Results

3.1. Resulting microstructure after printing and heat treatment

Fig. 3 shows the reconstructed SXCT slices of AP sample. In the bright contrast the inclusions with high Zr content can be identified. Zr inclusions are present in two shapes: (i) round particles (retained from initial powder as inclusions) and (ii) irregular shape particles or smaller micro-precipitates. The chemical composition of the latter was further studied by SEM in more details. Few inclusions/precipitates with density between pure Al and pure Zr (tentatively Al_2O_3 or TiC) are visible in the light grey; porosity is visible in black.

For quantitative image analysis all phases could be segmented, and their distribution and volume fraction were calculated. Al_2O_3/TiC inclusions had a volumetric content of 0.05 %, while all Zr inclusions had around 0.45 % and porosity was around 0.2 %. Since the initial amount of added Zr particles was 3 wt% (approx. 1.2 vol%), one can deduce that part of them have molten and dissolved into the matrix (shown previously up to 0.6–0.7 wt% Zr [9,10]). However, since many particles are left (Fig. 4a) one could assume that there was not enough energy input in the process to completely melt and dissolve Zr. This could possibly lead to inhomogeneous distribution of particles along the BD. However, the data analysis of local volume fraction of Zr particles obtained by SXCT did not show any particular inhomogeneity towards one side of the specimen along the BD (Fig. 4b), but rather a periodic distribution of Zr with local values varying from 0.2 % to almost 0.9 %. This could be a result of remelting phenomenon occurring due to the layer-by-layer PBF-LB processing.

Both AP and HT samples were then introduced in polished condition to an electron microscope. It was observed that both the microstructures were rich in inclusions, precipitates, and a few defects. The common observation for both sample conditions was one type of precipitates/inclusions containing Zr, which varied in size by several orders of magnitude: beginning with large globular inclusions of around 10–20 μm to very small nanometric precipitates (~0.1–0.3 μm). As seen in Fig. 5, the AP microstructure consisted of a variety of inclusions and precipitates with Zr as a common constituent; in fact, three categories of Zr-containing inclusions were characterised. The category 1 was recognized and confirmed as pure Zr inclusions, which are close in shape and size to pure Zr powder. Category 1 includes unmolten Zr-inclusions; such inclusions are thought to belong to regions where the heat could not melt them completely. Category 2 includes semi-molten Zr particles, and a number of Zr-Al phases formed at the interface with the Al-matrix. Such phases are formed upon partial melting of Zr powder particles and reaction with Al-melt/particles, as demonstrated in Fig. 6 and Fig. 7. Category 3 includes the Zr-rich precipitates that form upon direct solidification from the melt upon rapid cooling of Zr in Al. High-resolution EDS point scans (3 each) suggested clear enrichment of Zr in the two precipitates of category 3. Some of these precipitates (cubic Al_3Zr morphology) act as heterogeneous nucleation sites for solidification of Al-grains, thus favouring grain refinement [27,28]. Because of their size, only the precipitates with categories 1 and few from category 2 could be visible by SXCT (as shown in Fig. 3 and Fig. 4). This could explain a slightly conservative volume fraction estimates for

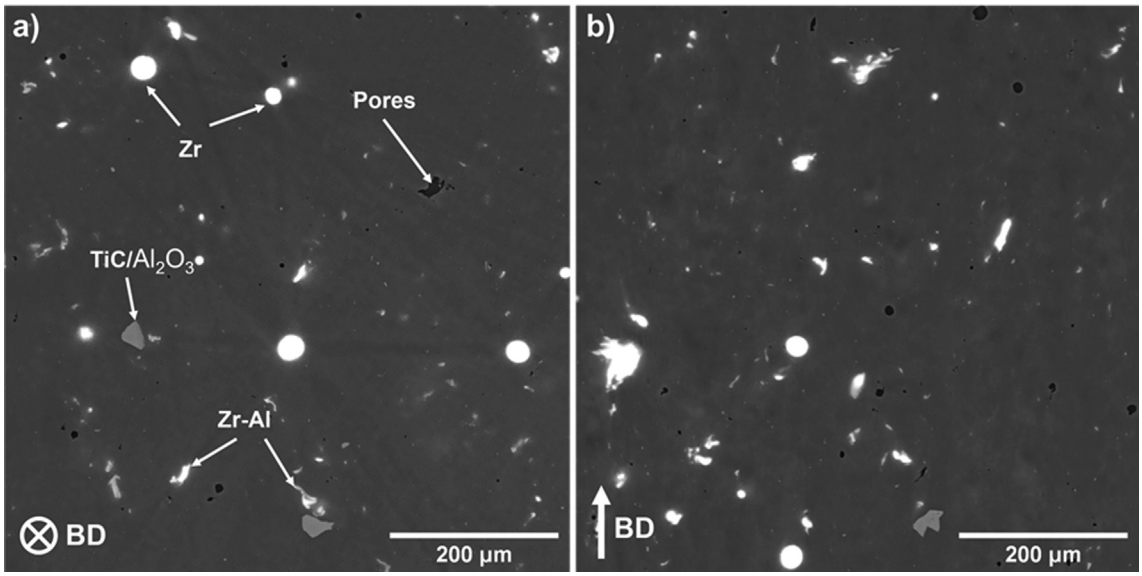

Fig. 3. SXCT reconstructed slices of AP sample a) in the build plane, b) perpendicular to the build plane.

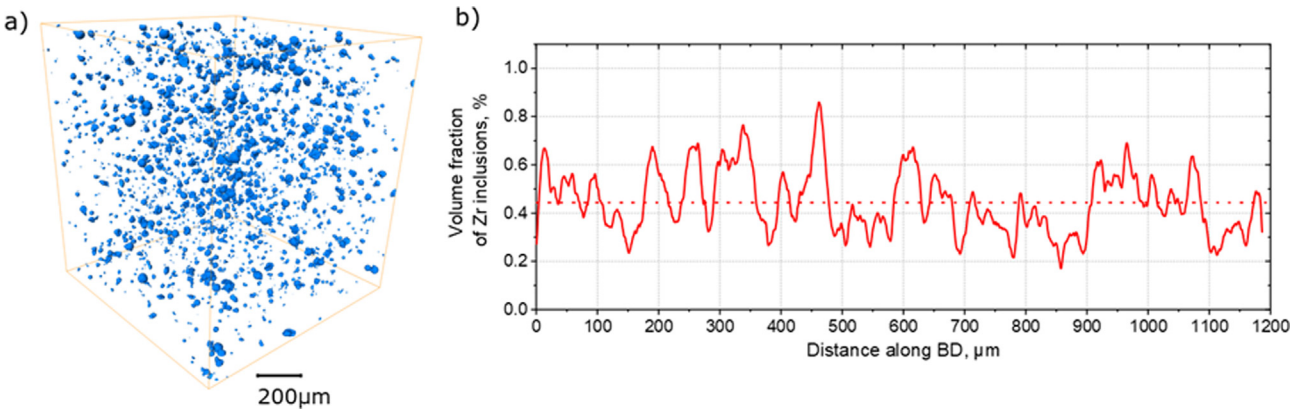

Fig. 4. A) 3D rendering of Zr inclusions, b) the volume fraction of Zr inclusions as a function of the distance along BD.

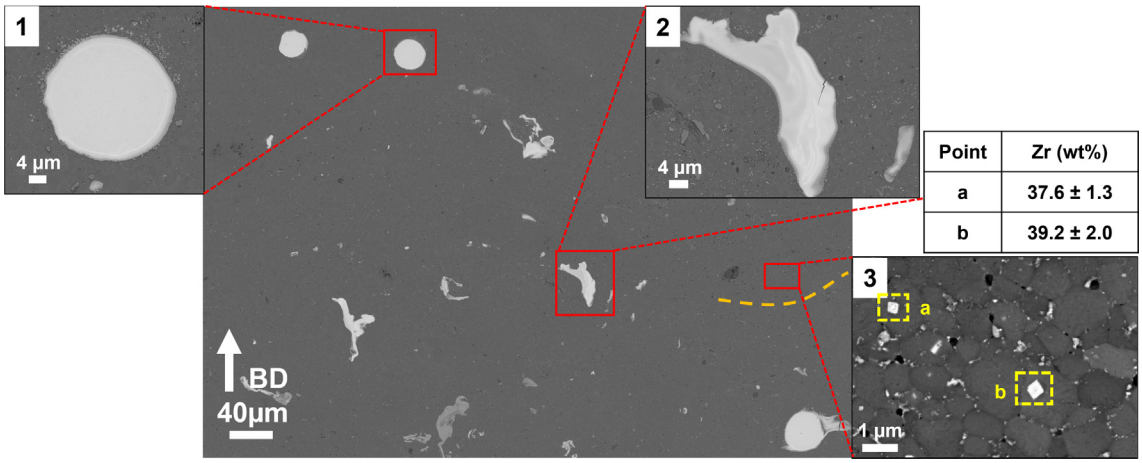

Fig. 5. Electron microscopy image along build direction of heat-treated sample showing the three categories of Zr precipitates namely unmolten (category 1), semi-molten (category 2) and fully molten (category 3) respectively.

Zr from SXCT data. Upon studying the unmolten and semi-molten Zr particles (categories 1 and 2) in more detail, see Fig. 6, it was seen that most of them contained microcracks at the interface with Al-matrix in both AP and HT conditions. This suggests that these cracks originate from the printing process and do not change upon heat treatments. Upon further investigation with the help of EDS chemical analysis conducted on several of these particles and illustrated in Fig. 7, it was seen that category 1 or 2, Zr-containing particles could have several different Al-Zr phases formed. This is clearly due to low energy and time available during the printing process to fully melt the Zr powder and dissolve the Zr in Al-matrix, thus forming several phases.

The other characteristic of the microstructure are grain boundary precipitates rich in Zn, Mg and Si. These elements usually form low-melting precipitates. Such precipitates accumulate at grain boundaries during the solidification process, as shown in Fig. 8 and Fig. 9 [29,30]. They can be dissolved in the matrix using solution heat treatment. Besides the precipitation reactions, the microstructure stays consistent at some locations after heat treatments. For example: The Zr inclusions seen in Fig. 5 are in a similar condition after heat treatments in the matrix. However, there are four major changes expected in the microstructure after heat treatment namely:

1. After solution heat treatments, most of the Zn-Mg precipitates are dissolved and then re-precipitate as nanometric GP Zones [31] in the grain interiors and grain boundaries. These mechanisms are well studied in literature [1,29,31].
2. The Zr dissolved in the matrix would re-precipitate as nanometric $L1_2$-Al_3Zr precipitates during solution treatment; this phenomenon is well documented to provide increase in yield strength [27,28].
3. The pores/ oxides increase in visibility as also shown in the Fig. 10 and confirmed via EDS presented in Fig. 11. Such oxides have been observed by other authors [32,33]. Some of the oxides were enriched in Si and Mg.
4. Few grain boundary precipitates enriched in Fe or Mg-Si were observed, as seen in Fig. 11a. It is suggested that these phases may be Al-Fe based or Mg_2Si precipitates formed during solidification, but they may have been overlooked in as-printed samples as most of the precipitates at grain boundaries were observed to be enriched in Zn-Mg or Mg-Si.

Finally, a few aluminium oxide precipitates (Al_2O_3) and TiC inclusions were also found in the samples for both conditions. The presence of Al_2O_3 suggests the pick-up of oxygen from the printing atmosphere or the formation from oxide layers on Al-powder. Interestingly, some of the oxides were seen to be decorated with smaller precipitates enriched in Ti,C and sometimes Zr. Some TiC inclusions were found in the matrix, which should originate from the admixed TiC particles. Electron microscopy images for the same can be found in the supplementary material. The sizes of Al_2O_3 suggest that they may be on the detection limit for SXCT whereas TiC inclusions are probably not detectable via SXCT.

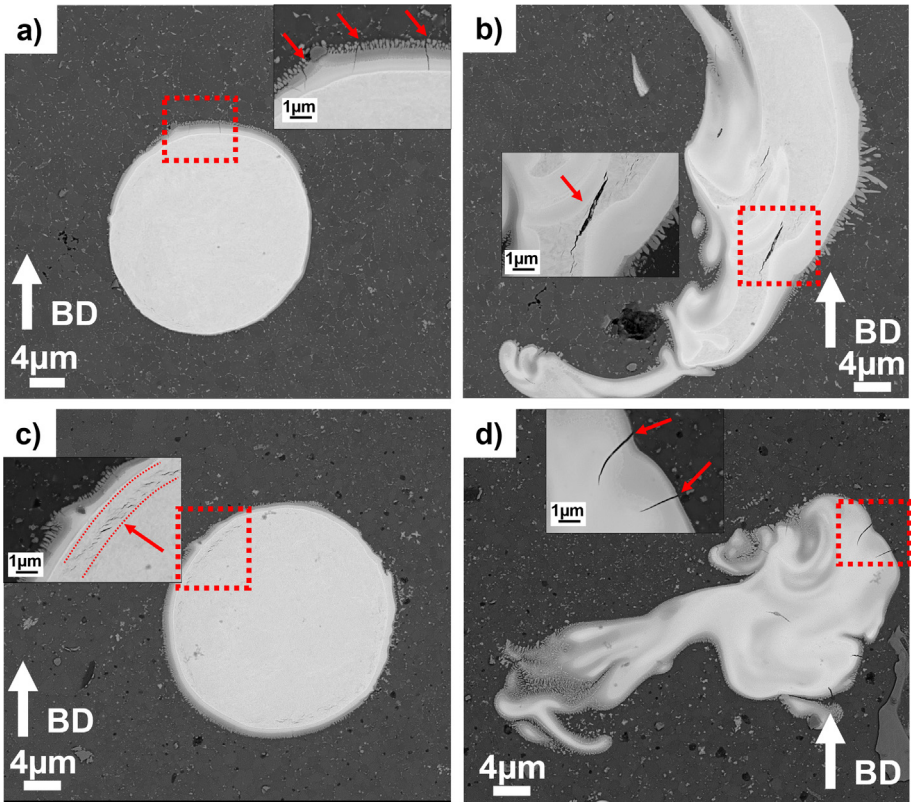

Fig. 6. Electron microscopy along build direction of AP sample with a) an intact Zr-powder particle and b) semi-molten Zr powder particle c)-d) Heat treated sample with an intact and semi-molten Zr particle respectively. All images give clear indications that microcracks are generated during the printing process.

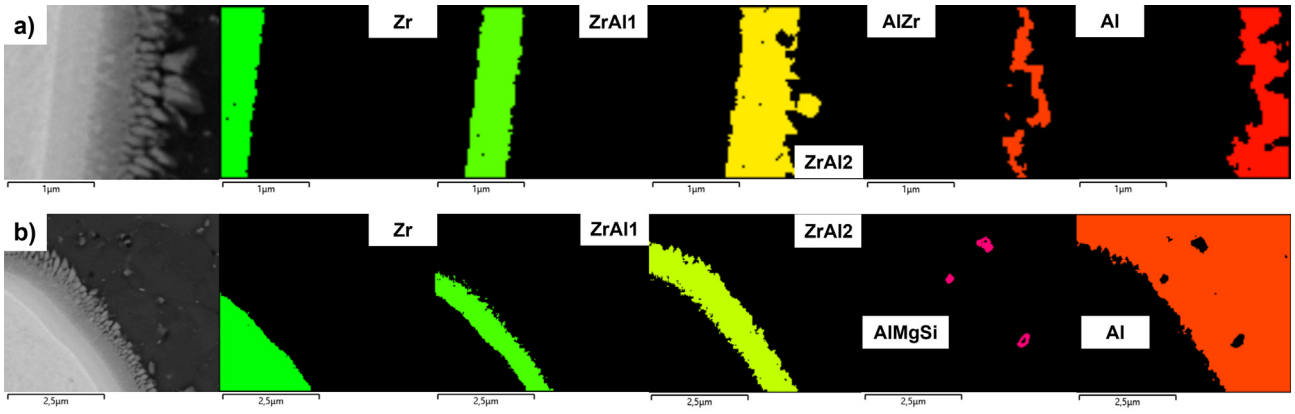

Legend

Precipitate	Constituents	Ratio of constituents (wt%, average)
Zr	Pure Zr	100
Al	Pure Al	100
ZrAl1	Zr-Al phase	Zr:Al ~ 80:20
ZrAl2	Zr-Al phase	Zr:Al ~ 50:50
AlZr	Al-Zr phase	Zr:Al ~ 20:80
AlMgSI	Mg-Si phase	

Fig. 7. High resolution EDX map showing different Al-Zr containing phases formed upon melting of Zr particles. Several types of Al:Zr ratio (wt%) are formed at different regions.

3.2. Tensile testing

Fig. 12 shows the stress–strain curves obtained during standard ex-situ tensile test (Fig. 12a). For AP samples, Young's modulus (GPa), yield strength (Rp0.2, MPa), ultimate tensile strength (Rm, MPa) and elongation to failure (%) of 84.9 GPa, 254 MPa, 303.5 MPa and 19.8 % are observed respectively. For HT samples, the same values averaged over two samples are 82.5 GPa, 444 MPa, 462.8 MPa and 8.9 % respectively. Stress–strain curves obtained during in-situ tensile test are shown in Fig. 12b. The star

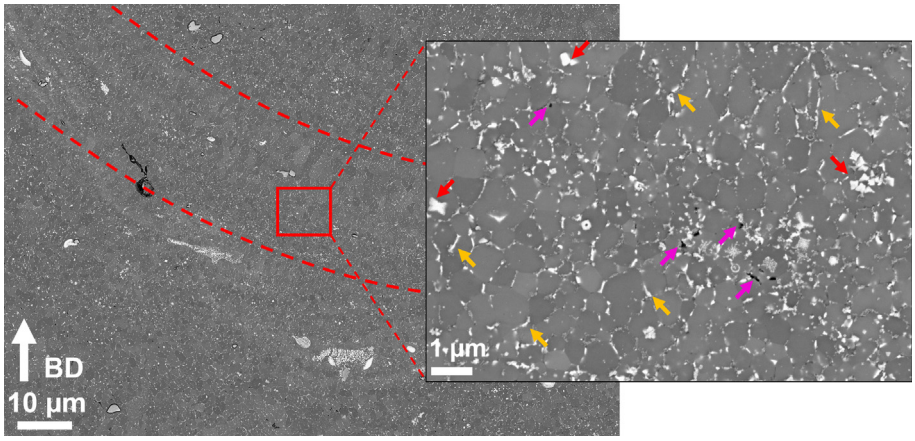

Fig. 8. Electron microscopy image along the building direction of AP sample showing two melt pool boundaries (marked in red) and grain refinement. Three types of microstructural features visible at higher magnifications marked as red, orange, and pink. They represent cubic Al_3Zr, grain boundary Zn-Mg precipitates and pores/oxides respectively. (For interpretation of the references to colour in this figure legend, the reader is referred to the web version of this article.)

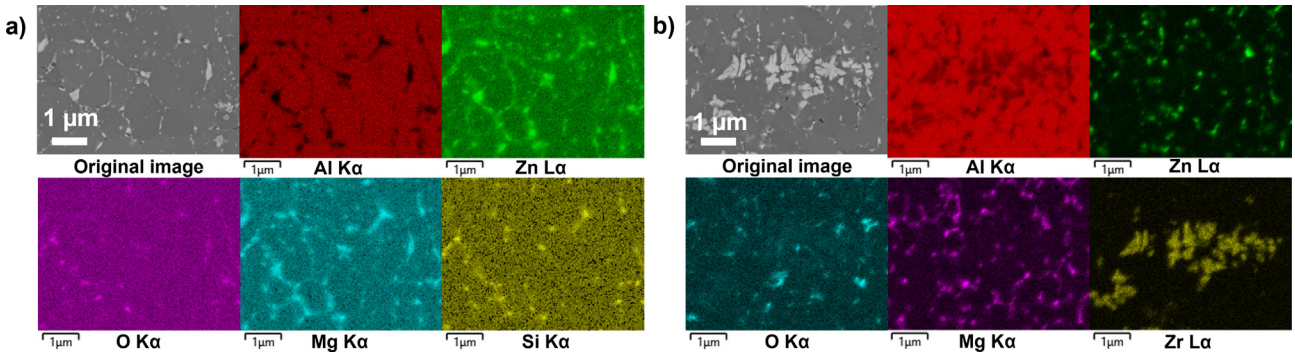

Fig. 9. High resolution EDS analysis for two regions of interest along building direction of AP sample a) Shows EDS chemical maps of regions highlighting grain boundaries with clear Zn-Mg precipitates segregated at grain boundaries with some Si, O containing precipitates, which could be oxides b) Shows EDS chemical maps focusing on the smaller Al_3Zr precipitates showing a clear segregation of Zr at these areas. Also, grain boundary Zn-Mg precipitates can be seen, similar to a).

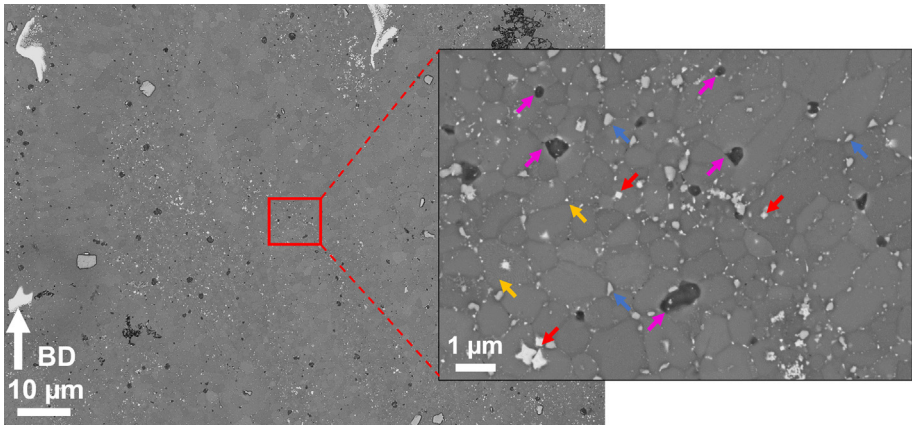

Fig. 10. Electron microscopy image along building direction of HT sample showing that grain sizes remain small (within 1–2 µm). Four categories of microstructural features visible at higher magnifications namely cubic Al_3Zr (red), re-precipitated Zn-Mg precipitates (in grain interiors; orange), pores/oxides (pink), and Fe-enriched grain boundary precipitates (blue). (For interpretation of the references to colour in this figure legend, the reader is referred to the web version of this article.)

symbols on the in-situ curves represent the load/displacement levels where SXCT scan was acquired. Despite the different sample geometries, set-up, and interruptions for SXCT scans, the two experiments show similar tensile behaviour with negligible strain hardening.

Fig. 13 (2D slices) and Fig. 14 (3D rendering of defects) summarize the damage evolution in AP samples during in-situ tensile test at the different load/displacement steps. Few lack-of-fusion defects can be observed inside the sample. One of them were open to the surface, as visible from the 3D rendering of the segmented defects (Fig. 14); such defects acted as an initiation site for the fracture. Globally, the crack grows and propagates in connection to the lack-of-fusion defects. However, locally it can be observed that the crack follows the borders of Zr inclusions (Fig. 13e,f in which

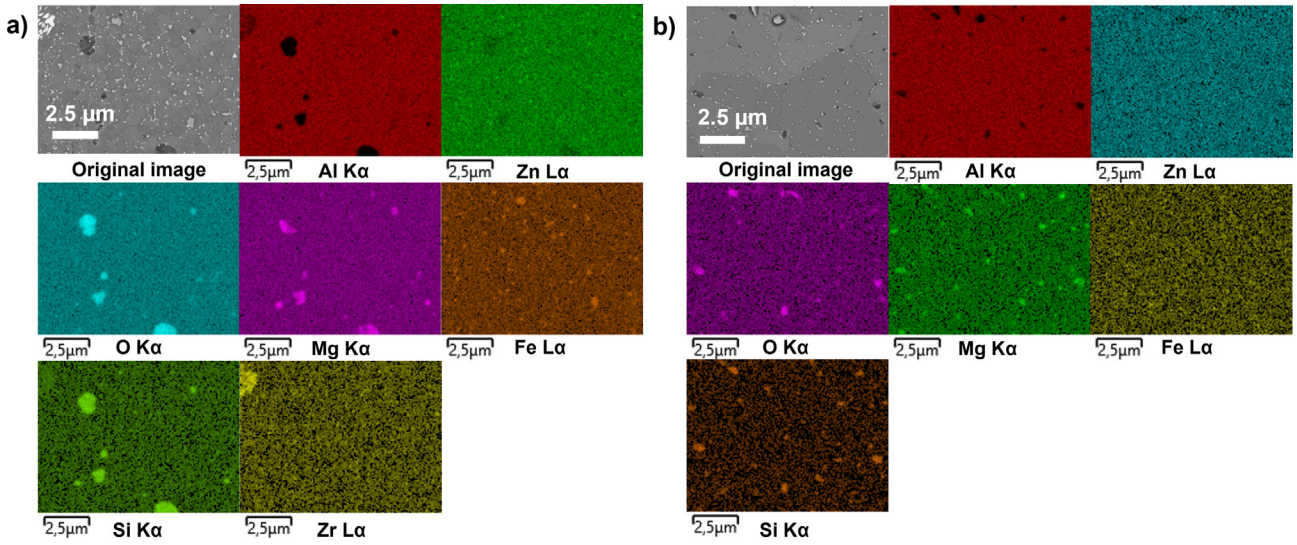

Fig. 11. EDS analysis done at high resolution for two regions of interest along building direction of HT sample a) EDS maps in regions highlighting area with pores/oxides, showing enrichment of oxygen, combined with Si and Mg. Some Fe precipitates were also seen, most around grain boundaries b) EDS map with smaller pores/oxides. Enrichment of Mg, Si, O at the smaller precipitates with darker contrast, that can be either oxides or Mg_2Si precipitates.

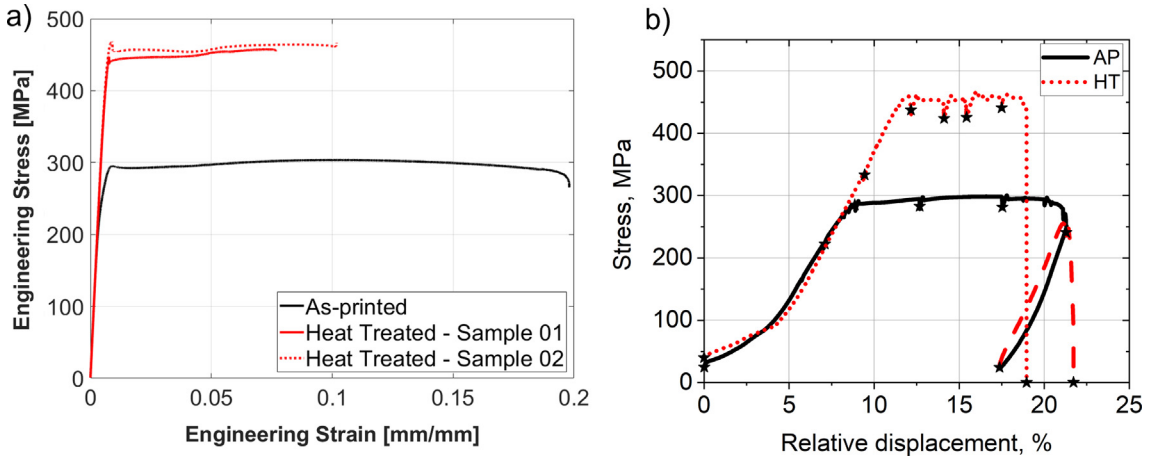

Fig. 12. A) Ex-situ standard stress–strain curve conducted in AP and HT, b) In-situ stress strain curve of AP condition and HT condition. Star symbols represent the displacement levels at which SXCT was performed.

Zr inclusions are those with bright contrast), which, therefore, deflect the crack propagation route at some points. The same behaviour was also observed for HT samples (see supplementary data).

3.3. Fracture characteristic inspection after ex-situ tensile testing

After ex-situ tensile testing, the samples were sectioned and prepared close to the necking area to study the fracture characteristics and explore the cause of failure. In both the AP and HT samples, as shown in Fig. 15, it is evident that the microcracks observed at the interface of Zr particles by means of electron microscopy (Fig. 6) have been sites for crack linking and propagation during tensile loading. This observation is similar to observations made from *in-situ* tensile testing. Similar observations were done for fracture section of heat treated samples as shown in Fig. 16. Secondly, it is well known that precipitate free zones (PFZs) are formed upon heat treatment of 7-series aluminium alloys [31]. These zones are soft regions close to grain boundaries, characterised by being depleted in precipitates. Such zones thus have low strength and are typically subjected to preferential local straining upon loading. Such strain localization causes in turn some reduction in ductility upon heat treatment. Since grain refinement occurs in this Al-alloy the grain boundary area increases; such phenomenon could enhance the deleterious effect of PFZs. A potential failure at grain boundaries is shown in Fig. 16 wherein the fracture linked across several grain boundaries. This potential phenomenon could be one important reason for the reduction of ductility from ~ 20 % in as-printed to ~ 9 % in heat-treated condition.

4. Discussions

This study elucidates a novel Al-alloy combining high strength with high stiffness. The alloys have been shown to be printable via PBF-LB process resulting in ~ 99.8 % relative density confirmed by SXCT & optical microscopy. To make the alloy system practically viable for applications demanding such properties, it is important to understand and explain the reason for fracture in these alloys. Such an investigation is deemed hard as it is nearly impossible to study the formation and growth of fracture surface in a material

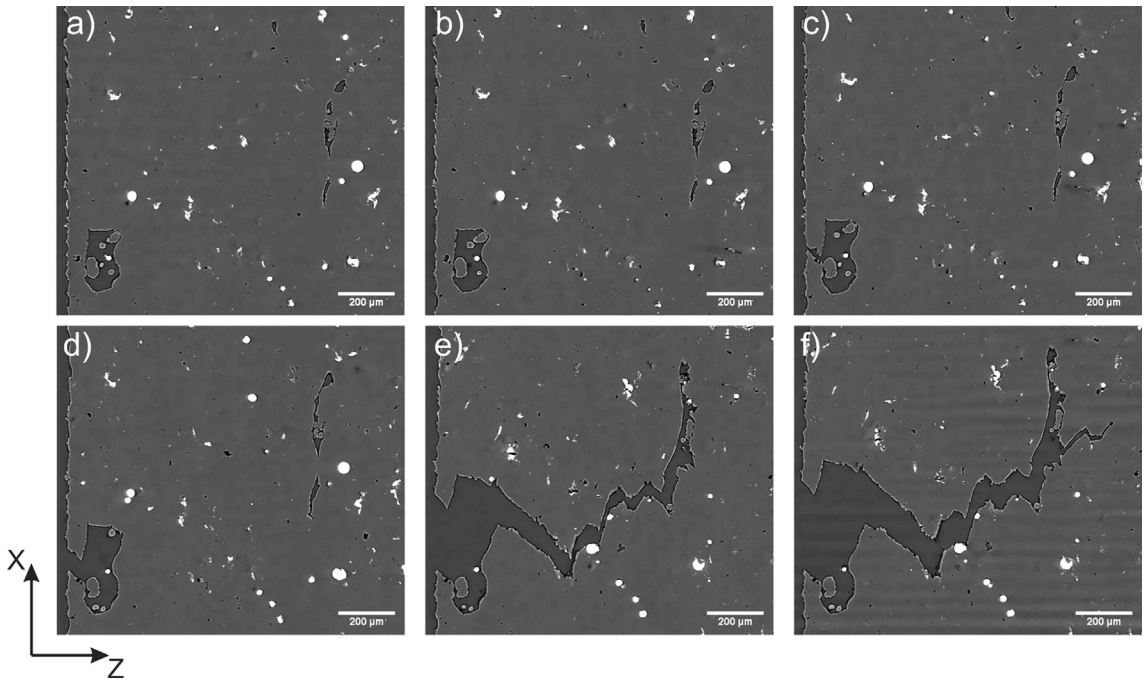

Fig. 13. Reconstructed SXCT slices of AP sample at different applied stress/displacement: a) initial, b) at 290 MPa (yield point), c) 5.5 % of plastic strain, d) 10 % of plastic strain, e) 15 % of plastic strain, f) before failure. *Z axis corresponds to BD.*

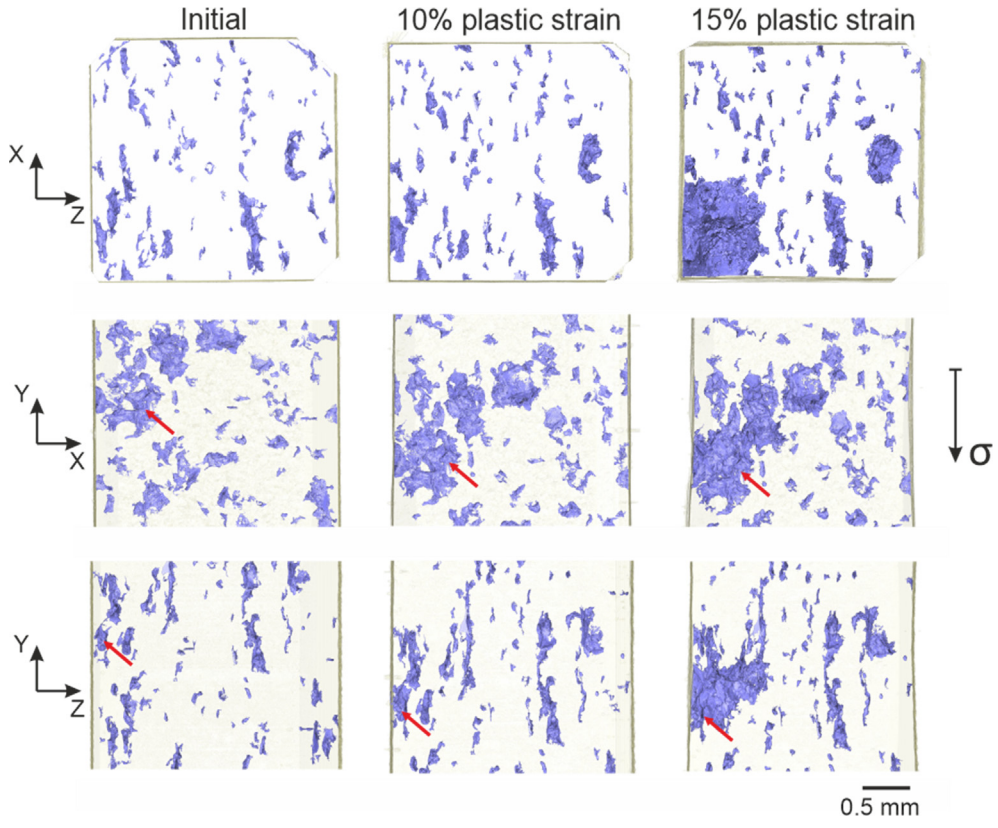

Fig. 14. The projection of the 3D rendering of pores in AB sample to XZ, XY and YZ planes. *Note: only 50 largest defects are shown, and Z axis corresponds to BD. Red arrows indicate the same location at different strain levels.* (For interpretation of the references to colour in this figure legend, the reader is referred to the web version of this article.)

during tensile loading. However, with the help of advanced in-situ tensile testing enabled at BAMline, the authors were able to investigate the crack initiation and possible reason for crack propagation in these alloys during as-printed and heat treated conditions. As summarized in Fig. 12, the tensile testing in all the cases was conducted on samples with loading perpendicular to build direction. During in-situ tensile testing, the experiments (Fig. 13 and Fig. 14) revealed that the failure initiated from a defect in the sam-

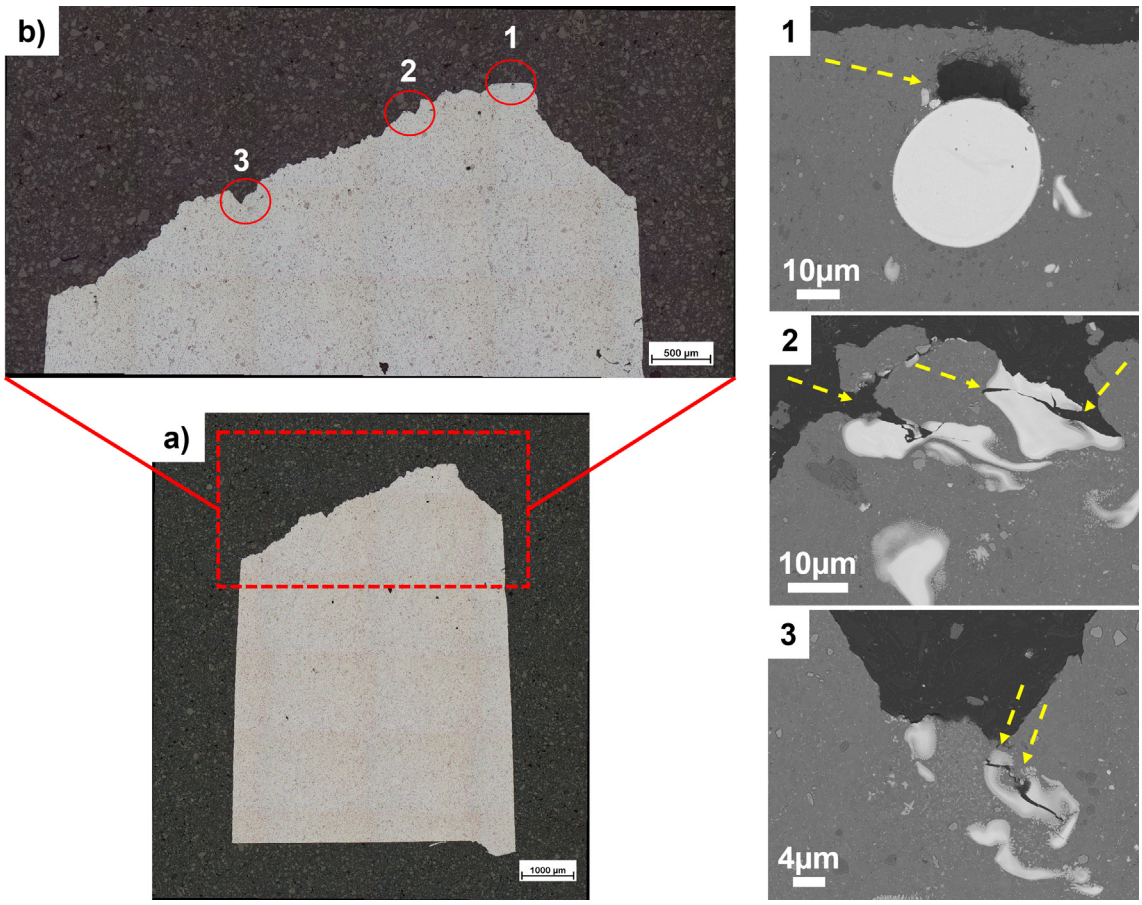

Fig. 15. Cross section of fracture surface of as-printed sample showing decohesion and further crack propagation at Al-Zr precipitate sites.

ple, which is a lack of fusion pore. The same defect was not confirmed during SXCT and electron microscopy of the printed cubes in both as-printed and heat treated conditions. One possible reason could be stochastic defects formed during printing of the samples [34,35]. These defects are unpredictable in nature and when large enough could affect the mechanical behaviour of the samples. The lack of fusion illustrated before in Fig. 14 could act as a site for crack initiation in plastic tensile regime and thus cause a premature failure as compared to AP samples thereby reducing ductility. Fig. 15, Fig. 16 and Fig. 17 show decohesion of Al-Zr particles arising from both unmolten and semi-molten conditions, which is confirmed with in-situ and ex-situ tensile testing methods. These fracture sites seem to depict that failure is deflected by the decohesion boundaries at Zr-Al interfaces, which is confirmed via both in-situ tensile testing and ex-situ fracture analysis. Consequently, even though crack initiation happened due to a stochastic defect in the sample, the propagation of the crack was controlled via deflections along the cross section of the sample owing to Al-Zr inclusions. This could help enhance the ductility of the material for both the as-printed condition and possibly the heat treated condition. This could also explain the high ductility of ~ 20 % for the in-situ sample in spite of having few lack of fusion defects. However, during heat treatments, PFZs become an additional concern causing local softening around grain boundaries during plastic deformation thus affecting ductility. These are usually controlled via under-ageing or over-ageing the material for better ductility [29]. It is thus suspected that such inclusions could help improve the general mechanical properties of the alloys in one way. The printing defects may be eventually made better with good processing conditions to enhance material properties even further. However, the Zr-Al interfaces will always be there in such an alloy system as it is a consequence of the printing process.

The resulting mechanical property of this alloy is quite promising too. In as-printed condition, the alloys show an upper yield point around 295 MPa, which is also observed in other grain refined Al-alloys processed via PBF-LB [6,33,36,37]. This upper yield point is followed by a load drop, thus leading to a possible Lüders band formation. On heat treating the alloy, a total increase of yield strength from 254 MPa to 444 MPa is shown, which is about 75 % increase in yield strength with a small reduction in Young's modulus from 85 GPa to 82.4 GPa. The elongation to fracture reduces from ~ 20 % in as-printed condition to ~ 8–10 % elongation. A negligible Portevin-Le-Chatelier (PLC) was observed in both the conditions, unlike what is observed in several Al-Mg rich PBF-LB alloys [9,33]. This could be linked to unavailability of Mg in solid solution due to formation of Mg-rich precipitates (Zn-Mg or possibly Mg-Si) in both cases as shown in Fig. 9 and Fig. 11. The yield strength ratio (Rp0.2/Rm) for AP and HT conditions are 0.83 and 0.96 respectively. This suggests a relatively lower strain hardening in these alloys as compared to conventional high-strength Al-alloys such as 2024, 7075 etc. where this ratio is 0.80–0.90 in heat treated condition as compared to 0.96 in this alloy [1]. As per [36], such a phenomenon is attributed to refined grain structure which means that dislocation hardening via dislocation pile-up during plastic deformation becomes ineffective due to high amount of grain boundaries. Overall, this performance seems to be better than conventionally produced 7017 Al-alloys with ~ 20 % higher Young's modulus combined with a similar elongation to failure and competitive yield strength as other conventionally produced 7000-series Al-alloys [1,38]. However, to

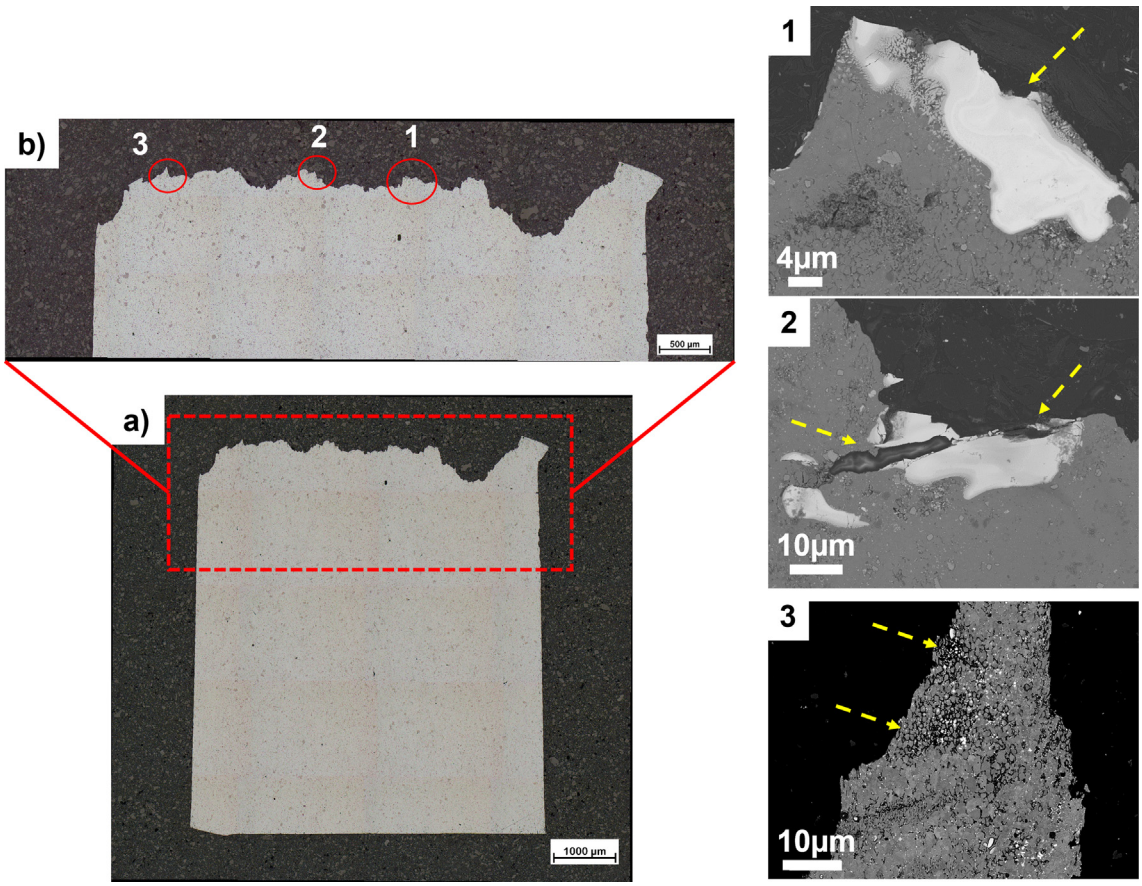

Fig. 16. Cross section of fracture surface of heat treated sample showing decohesion at Al-Zr inclusions and grain boundary cracking caused due to typical PFZs.

statistically quantify the mechanical performance of these alloys, more samples would need to be tested. These superior mechanical properties are explained in terms of four microstructural feature present in the material namely primary Al-grain refinement, Zr-inclusions/precipitates, Zn-Mg/Mg-Si precipitates, and other precipitates/inclusions (such as TiC).

The primary Al-grain refinement is a necessary feature in the alloy to make it processable via PBF-LB process. If the solidification cracking susceptibility for these alloys are calculated (as mentioned elsewhere [10,39]), it can be seen that such 7017 Al-alloys have high cracking susceptibility. Formation of primary Al_3Zr during solidification [6,9] and presence of TiC powder in the melt [40] would act as heterogeneous nucleation sites leading to refined primary Al-grains thus avoiding solidification cracking. The resulting Al-grain refinement would also result in enhanced yield strength [41] due to well-known Hall-Petch effect. The effect of Zr-inclusions/precipitates is central to this alloy system. As mentioned before, primary Al_3Zr support grain refinement thus making it feasible to print these alloys in the first place. Moreover, the small amount of Zr that gets dissolved in the solid solution (~0.6 wt% [10]) could provide great improvements in strength via precipitation hardening following the solution heat treatment. This occurs due to formation of nanometric Al_3Zr precipitates, as seen by other authors [9,28,42,43]. The majority of the 3- wt% Zr is suspected to be left in the Al-matrix as unmolten or semi-molten Zr inclusions, as seen in Fig. 5. SXCT could confirm about 40 % of these Zr inclusions in as-printed and heat treated conditions, but it is suspected that even higher amounts could be present as some of the semi-molten Zr inclusions were beyond the detection limit of the tomography testing. Upon conducting high resolution EDS analysis, a compositional variation in terms of Zr enrichment is observed for a few micrometres from the interface, as shown in Fig. 7. This is explained via insufficient energy transfer from the laser beam during PBF-LB processing to completely melt Zr and thus caused the formation of different Zr-Al phases, based on how much Al could diffuse into Zr. These two elements show a response similar to the one observed on welding of dissimilar metals Fe and Al [44]. Several Fe-Al phases are formed at the interface region causing cracking. Such a phenomenon is undesirable in Fe-Al welding due to these phases being susceptible to galvanic corrosion and worse mechanical properties. Similar to Fe-Al, the authors observed microcracks at Zr-Al interfaces (shown in Fig. 6). Such microcracks result from solidification cracking phenomenon occurring due to separation into multiple phases, thus having a higher susceptibility to solidification cracking as illustrated in the Scheil solidification curve for Al-Zr binary system in Fig. 18. Unexpectedly, these microcracks were confirmed to hinder the crack propagation during tensile loading, as confirmed both via in-situ and ex-situ tensile testing. It is only due to non-destructive nature of in-situ testing shown in Fig. 13 and Fig. 14 that a clear evidence could be established for the nature of such inclusions. Thus, it is shown that these inclusions help in improving ductility by deflecting the crack propagation during plastic tensile regime.

The third characteristic features of the microstructure are the Zn-Mg or Mg-Si enriched precipitates around grain boundaries (Fig. 9). Such precipitates are typical to form with 7000-series aluminium alloys, although it is observed that Zn-Mg and Mg-Si primary precipitates are quite refined (by an order of magnitude) when processed via PBF-LB as compared to the conventional Al-alloy counterparts. Thus, they could contribute to strength in as-printed condition, which is not the case for conventional 7000-series Al-alloys when these precipitates are formed in 1–10 µm

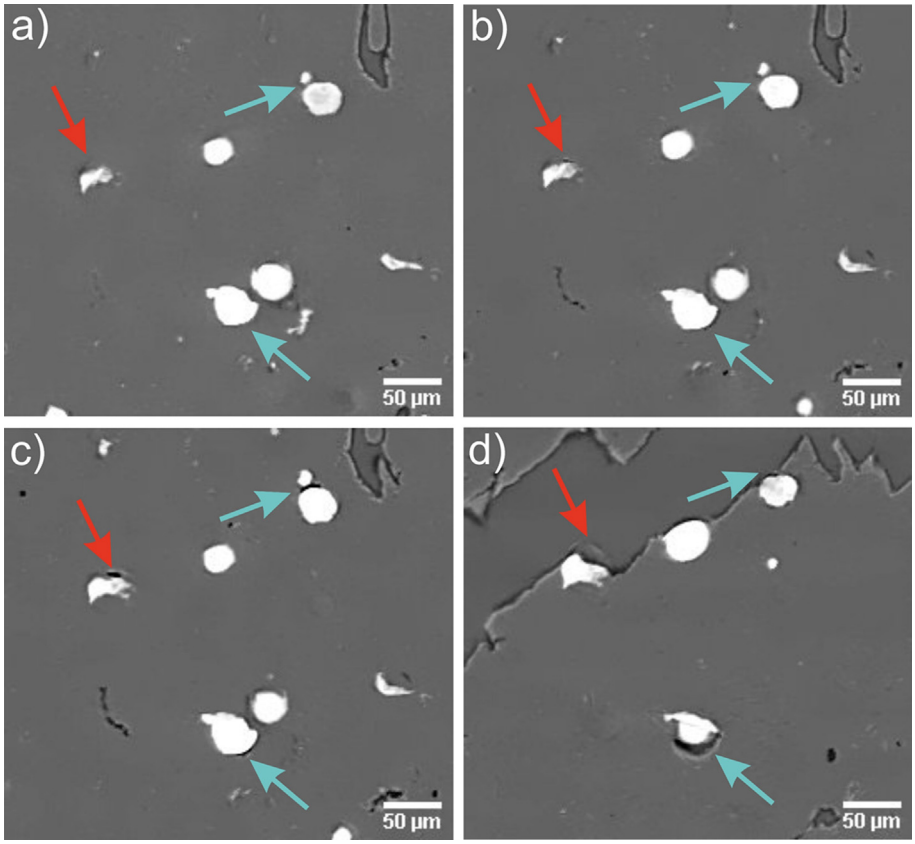

Fig. 17. Reconstructed SXCT slices of AP sample at different applied stress/displacement: a) initial, b) 290 MPa (yield point), c) 15 % of plastic strain, d) before failure. The decohesion is indicated by arrows.

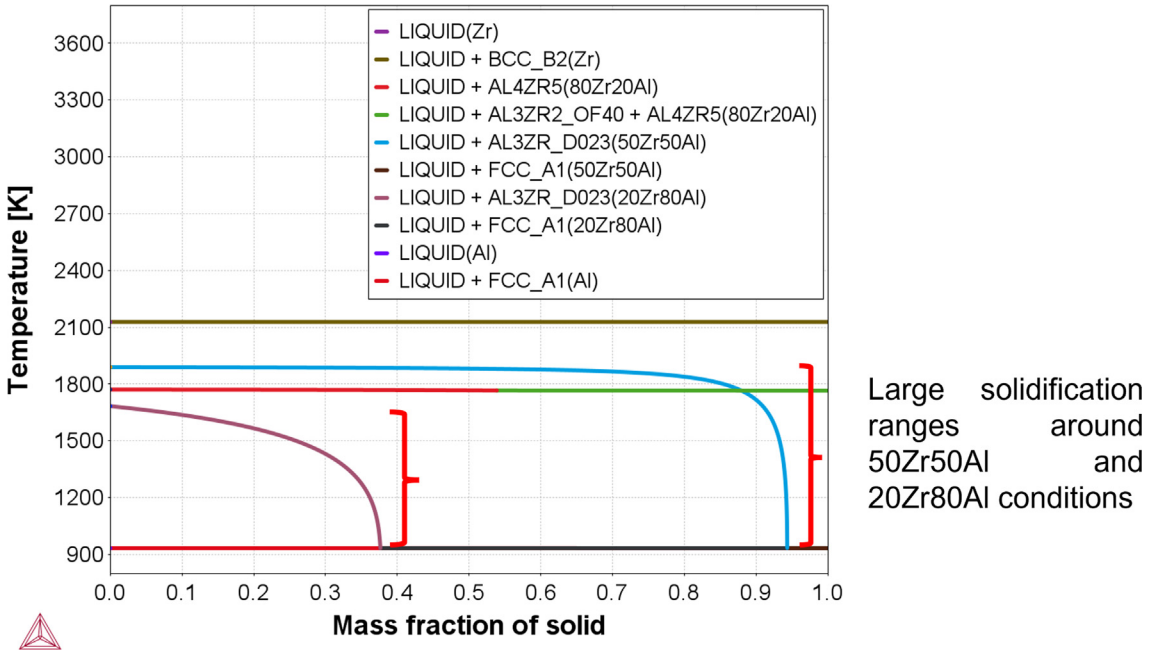

Fig. 18. Scheil solidification [45] for five conditions with different Al-Zr phases namely Zr (100 wt% Zr), 80Zr20Al (80 wt% Zr, 20 wt% Al), 50Zr50Al (50 wt% Zr, 50 wt% Al), 20Zr80Al (20 wt% Zr, 80 wt% Al), Al (100 wt% Al). Solidification range can be up to 1000 K (for 50Zr50Al condition), which could cause heavy solidification cracking.

size range [1]. This refined microstructure formed upon printing also affects the heat treatment procedure. It allows these alloys for much low time for solution heat treatment to dissolve the primary precipitates from 5 to 6 h for conventional Al-alloys to 1 h for PBF-LB [29]. During the second step of heat treatment, nano scale GP zones are formed which would increase the yield strength via precipitation hardening. However, these nano scale GP zones are formed inside the grains or at grain boundaries due to faster diffu-

sion of solutes, thus leaving a small channel of precipitate free zones (PFZs) [31] which contributes to a loss in ductility of such alloys after heat treatments. PFZs could be hard to detect with in-situ tensile testing due to the refined grain structure making the cracks very small and diffused. An illustration was observed in the cross section of fracture surface in Fig. 16b wherein the third inset shows severe cracking in refined grain region of the sample. Such a failure could be a result of PFZs creating local soft zones and the crack propagating through them. However, since the grains were sub-micron sized, such a phenomenon would be hard to catch during in-situ tensile testing.

There are a few solutions that could help reduce or completely remove the amount of defects that are not improvable by modifying processing conditions, namely:

1. The increase in Young's modulus could be resulting through contributions from Zr particles (Young's modulus pure Zr = 94.5 GPa) in the alloy, acting as reinforcements similar to metal matrix composite (MMC) materials. Such Zr particles could be finer in size before adding to the base alloy to ensure more heat transfer to Zr thus improving such issues.
2. Zr could be added during atomisation of Al 7017 powder. It has been shown that about 0.6–0.7 wt% Zr is dissolvable, and the rest will eventually precipitate in primary Al-matrix [9,10,46].
3. Other semi-stable methods such as coating powder with ZrH_2 has been shown to be successful [6] and could be tried to boost Zr contents in the alloy.

These alloys combine a high strength (~445 MPa Yield strength) with reasonable elongation (~10 %) and high Young's modulus (>80 GPa), producing mechanical properties better than their conventionally produced counterparts [1,38]. Looking at Fig. 19 such alloys could be very interesting in finding applications replacing Al-based MMC materials or conventionally produced high-strength Al-alloys. As typical for MMC, the studied material has a relatively higher Young's modulus. Unlike the conventional MMCs [48–49], elongation to failure is much better in these novel Al7017 materials combined with better yield strengths, thus utilising an "empty space" in the Ashby chart. Such alloys could be lucrative in applications where higher stiffness is required such as robotic arms, or products having stiffness limited designs.

5. Conclusions

- This study introduces a novel 7017 grade Al-alloy admixed with 3 wt% Zr and 0.5 wt% TiC, which gives it a crack-free, fine-grained complex microstructure. This microstructure is primarily enriched with different Al-Zr phases. Some of these phases were prone to microcracks at the interface between the particles and Al-matrix.
- The critical part of this study is the in-situ tensile testing at synchrotron facility (BAMline, Berlin) with complementary ex-situ tensile testing in a standard tensile test at Chalmers University. Comparing the results, a clear trend is seen wherein crack initiation occurs at stochastic defects for both cases (as-printed and heat treated). The crack propagation in both cases is attributed primarily to Al-Zr inclusions found in the Al-matrix. This observation is expected to enhance the ductility of the material by deflecting cracks during plastic deformation. In heat treated conditions, formation of precipitate free-zones also impacts ductility negatively.
- Both conditions (as-printed, heat treated) suggest good mechanical properties in the material are derived from microstructural features such as abovementioned Al-Zr phases, refined Al-grains and Zn-Mg/Mg-Si precipitates showing Young's modulus > 80 GPa and yield strengths up to 445 MPa in HT condition.

Data availability

Data will be made available on request.

Declaration of Competing Interest

The authors declare that they have no known competing financial interests or personal relationships that could have appeared to influence the work reported in this paper.

Acknowledgements

The authors would like to acknowledge the support in terms of funding from Centre for Additive Manufacturing-Metal (CAM2) hosted by Chalmers University of Technology, supported by VINNOVA (grant number: 2016-05175). The authors would also acknowledge Dr. Elanghovan Natesan at Chalmers University for conducting tensile tests.

Appendix A. Supplementary data

Supplementary data to this article can be found online at https://doi.org/10.1016/j.matdes.2023.111602.

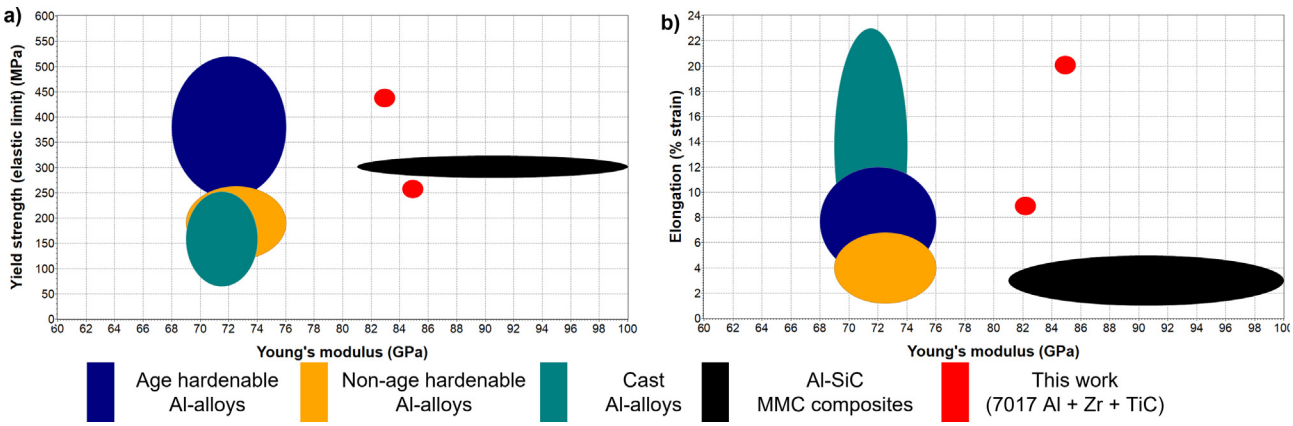

Fig. 19. Ashby charts [16] showing a) Young's modulus (GPa) vs yield strength (MPa) and b) Young's modulus (GPa) vs elongation to failure (%).

References

[1] ASM International. Introduction to Aluminum and Aluminum Alloys, *Metals Handbook Desk Edition*, 1998, pp. 417–423, doi: 10.31399/asm.hb.mhde2.a0003121.

[2] T. DebRoy et al., Additive manufacturing of metallic components – Process, structure and properties, Prog. Mater Sci. 92 (2018) 112–224, https://doi.org/10.1016/j.pmatsci.2017.10.001.

[3] B. Blakey-Milner et al., Metal additive manufacturing in aerospace: A review, Mater. Des. 209 (2021), https://doi.org/10.1016/j.matdes.2021.110008 110008.

[4] H. Hyer et al., Elimination of extraordinarily high cracking susceptibility of aluminum alloy fabricated by laser powder bed fusion, J. Mater. Sci. Technol. 103 (2022) 50–58, https://doi.org/10.1016/j.jmst.2021.06.023.

[5] N.T. Aboulkhair, M. Simonelli, L. Parry, I. Ashcroft, C. Tuck, R. Hague, 3D printing of Aluminium alloys: Additive Manufacturing of Aluminium alloys using selective laser melting, Prog. Mater Sci. 106 (August) (2019) 100578, https://doi.org/10.1016/j.pmatsci.2019.100578.

[6] J.H. Martin, B.D. Yahata, J.M. Hundley, J.A. Mayer, T.A. Schaedler, T.M. Pollock, 3D printing of high-strength aluminium alloys, Nature 549 (7672) (2017) 365–369, https://doi.org/10.1038/nature23894.

[7] J.H. Martin, B.D. Yahata, E.C. Clough, J.A. Mayer, J.M. Hundley, T.A. Schaedler, Additive manufacturing of metal matrix composites via nanofunctionalization, MRS Commun. 8 (2) (2018) 297–302, https://doi.org/10.1557/mrc.2018.95.

[8] K. Schmidtke, F. Palm, A. Hawkins, C. Emmelmann, Process and mechanical properties: Applicability of a scandium modified Al-alloy for laser additive manufacturing, Phys. Proc. (2011), https://doi.org/10.1016/j.phpro.2011.03.047.

[9] J.R. Croteau et al., Microstructure and mechanical properties of Al-Mg-Zr alloys processed by selective laser melting, Acta Mater. 153 (Jul. 2018) 35–44, https://doi.org/10.1016/j.actamat.2018.04.053.

[10] B. Mehta, L. Nyborg, K. Frisk, E. Hryha, Al–Mn–Cr–Zr-based alloys tailored for powder bed fusion-laser beam process: Alloy design, printability, resulting microstructure and alloy properties, J. Mater. Res. 3 (2022) 1–13, https://doi.org/10.1557/s43578-022-00533-1.

[11] S. Thapliyal et al., An integrated computational materials engineering-anchored closed-loop method for design of aluminum alloys for additive manufacturing, Materialia (Oxf) 9 (December) (2020) 100574, https://doi.org/10.1016/j.mtla.2019.100574.

[12] K. Schmidtke, F. Palm, A. Hawkins, C. Emmelmann, Process and mechanical properties: Applicability of a scandium modified Al-alloy for laser additive manufacturing, Phys. Proc. 12 (PART 1) (2011) 369–374, https://doi.org/10.1016/j.phpro.2011.03.047.

[13] Q. Jia et al., Precipitation kinetics, microstructure evolution and mechanical behavior of a developed Al-Mn-Sc alloy fabricated by selective laser melting, Acta Mater. (2020), https://doi.org/10.1016/j.actamat.2020.04.015.

[14] J.L. Cann et al., Sustainability through alloy design: Challenges and opportunities, Prog. Mater Sci. 117 (July) (2021) 100722, https://doi.org/10.1016/j.pmatsci.2020.100722.

[15] A. Plotkowski et al., Microstructure and properties of a high temperature Al–Ce–Mn alloy produced by additive manufacturing, Acta Mater. 196 (2020) 595–608, https://doi.org/10.1016/j.actamat.2020.07.014.

[16] Michael F. Ashby, *Materials selection in mechanical design*, 2005.

[17] A. du Plessis, I. Yadroitsava, I. Yadroitsev, Effects of defects on mechanical properties in metal additive manufacturing: A review focusing on X-ray tomography insights, Mater. Des. 187 (2020), https://doi.org/10.1016/j.matdes.2019.108385 108385.

[18] S. Evsevleev, S. Paciornik, G. Bruno, Advanced Deep Learning-Based 3D Microstructural Characterization of Multiphase Metal Matrix Composites, Adv. Eng. Mater. 22 (4) (2020) 1–6, https://doi.org/10.1002/adem.201901197.

[19] Z. Wang et al., In-situ synchrotron X-ray tomography investigation of damage mechanism of an extruded magnesium alloy in uniaxial low-cycle fatigue with ratchetting, Acta Mater. 211 (2021), https://doi.org/10.1016/j.actamat.2021.116881 116881.

[20] I. Serrano-Munoz, D. Shiozawa, S. Dancette, C. Verdu, J.Y. Buffiere, Torsional fatigue mechanisms of an A357–T6 cast aluminium alloy, Acta Mater. 201 (2020) 435–447, https://doi.org/10.1016/j.actamat.2020.09.046.

[21] A. du Plessis et al., Prediction of mechanical performance of Ti6Al4V cast alloy based on microCT-based load simulation, J. Alloy. Compd. 724 (2017) 267–274, https://doi.org/10.1016/j.jallcom.2017.06.320.

[22] A. Rack et al., High resolution synchrotron-based radiography and tomography using hard X-rays at the BAMline (BESSY II), Nucl Instrum Methods Phys Res A 586 (2) (2008) 327–344, https://doi.org/10.1016/j.nima.2007.11.020.

[23] H. Markötter, M. Sintschuk, R. Britzke, S. Dayani, G. Bruno, Upgraded imaging capabilities at the BAMline (BESSY II), J. Synchrotron Radiat. 29 (5) (Sep. 2022) 1292–1298, https://doi.org/10.1107/S1600577522007342.

[24] S. Berg et al., Ilastik: Interactive Machine Learning for (Bio)Image Analysis, Nat. Methods 16 (12) (2019) 1226–1232, https://doi.org/10.1038/s41592-019-0582-9.

[25] D. Gürsoy et al., TomoPy: a framework for the analysis of synchrotron tomographic data, Journal of Synchrotron Radiation 21 (2014) 1188–1193, https://doi.org/10.1107/S1600577514013939.

[26] "Avizo Software," *Thermo Fisher Scientific*. https://www.thermofisher.com/se/en/home/electron-microscopy/products/software-em-3d-vis/avizo-software.html (accessed Aug. 31, 2022).

[27] K.E. Knipling, D.C. Dunand, D.N. Seidman, Criteria for developing castable, creep-resistant aluminum-based alloys - A review, Int. J. Mater. Res. 97 (3) (2006) 246–265.

[28] K.E. Knipling, D.C. Dunand, D.N. Seidman, Precipitation evolution in Al-Zr and Al-Zr-Ti alloys during aging at 450–600 °C, Acta Mater. 56 (6) (2008) 1182–1195, https://doi.org/10.1016/j.actamat.2007.11.011.

[29] T.H.E. Major, A. Alloy, Heat Treatment Practices of Age-Hardenable Aluminum Alloys *, vol. 4, no. c, 2016, doi: 10.31399/asm.hb.v04e.a0006288.

[30] G.E. Totten, D.S. Mackenzie, Principles of Heat Treating of Nonferrous Alloys *, vol. 4, 2016, doi: 10.31399/asm.hb.v04e.a0006250.

[31] K.E. Easterling, D.A. Porter, *Phase Transformations in Metals and Alloys*, second ed., Chapman & Hill, London, 1992.

[32] S. Griffiths et al., Coarsening- and creep resistance of precipitation-strengthened Al–Mg–Zr alloys processed by selective laser melting, Acta Mater. 188 (2020) 192–202, https://doi.org/10.1016/j.actamat.2020.02.008.

[33] A.B. Spierings, K. Dawson, K. Kern, F. Palm, K. Wegener, SLM-processed Sc- and Zr- modified Al-Mg alloy: Mechanical properties and microstructural effects of heat treatment, Mater. Sci. Eng. A 701 (June) (2017) 264–273, https://doi.org/10.1016/j.msea.2017.06.089.

[34] C. Schwerz, Detection and classification of internal flaws in laser powder bed fusion, 2021.

[35] Z. Snow, A.R. Nassar, E.W. Reutzel, Invited Review Article: Review of the formation and impact of flaws in powder bed fusion additive manufacturing, Addit. Manuf. 36 (January) (2020), https://doi.org/10.1016/j.addma.2020.101457 101457.

[36] M. Avateffazeli et al., Correlation between tensile properties, microstructure, and processing routes of an Al–Cu–Mg–Ag–TiB2 (A205) alloy: Additive manufacturing and casting, Mater. Sci. Eng. A 841 (January) (2022), https://doi.org/10.1016/j.msea.2022.142989 142989.

[37] Q. Jia et al., Selective laser melting of a high strength Al[sbnd]Mn[sbnd]Sc alloy: Alloy design and strengthening mechanisms, Acta Mater. 171 (Jun. 2019) 108–118, https://doi.org/10.1016/j.actamat.2019.04.014.

[38] P.K. Rout, M.M. Ghosh, K.S. Ghosh, Microstructural, mechanical and electrochemical behaviour of a 7017 Al-Zn-Mg alloy of different tempers, Mater Charact 104 (Jun. 2015) 49–60, https://doi.org/10.1016/j.matchar.2015.03.025.

[39] S. Kou, A criterion for cracking during solidification, Acta Mater. 88 (2015) 366–374, https://doi.org/10.1016/j.actamat.2015.01.034.

[40] K. Zhao et al., Enhanced grain refinement and mechanical properties of a high–strength Al–Zn–Mg–Cu–Zr alloy induced by TiC nano–particles, Mater. Sci. Eng. A 806 (Mar. 2021), https://doi.org/10.1016/j.msea.2021.140852.

[41] Z.C. Cordero, B.E. Knight, C.A. Schuh, Six decades of the Hall-Petch effect – a survey of grain-size strengthening studies on pure metals, Int. Mater. Rev. 61 (8) (2016) 495–512, https://doi.org/10.1080/09506608.2016.1191808.

[42] P. H. L. Souza, C. A. S. de Oliveira, and J. M. do V. Quaresma, Precipitation hardening in dilute Al–Zr alloys, *J. Mater. Res. Technol.* 7(1) (2018) 66–72, doi: 10.1016/j.jmrt.2017.05.006.

[43] B. Mehta, K. Frisk, L. Nyborg, Effect of Precipitation Kinetics on Microstructure and Properties of Novel Al-Mn-Cr-Zr Based Alloys Developed for Powder Bed Fusion – Laser Beam Process, J. Alloy. Compd. (2022), https://doi.org/10.1016/j.jallcom.2022.165870.

[44] M.d. Abdul Karim, Y.-D. Park, A Review on Welding of Dissimilar Metals in Car Body Manufacturing, J. Weld. Joining 38 (1) (Feb. 2020) 8–23, https://doi.org/10.5781/jwj.2020.38.1.1.

[45] E. Scheil, Bemerkungen zur schichtkristallbildung, Z. Metallkd. (1942).

[46] S. J. Griffiths, "Seth James GRIFFITHS," 2020.

[47] P. Samal, P.R. Vundavilli, A. Meher, M.M. Mahapatra, Recent progress in aluminum metal matrix composites: A review on processing, mechanical and wear properties, J. Manuf. Process. 59 (September) (2020) 131–152, https://doi.org/10.1016/j.jmapro.2020.09.010.

[48] S.V. Nair, J.K. Tien, R.C. Bates, Sic-reinforced aluminium metal matrix composites, International Metals Reviews 30 (1) (1985) 275–290, https://doi.org/10.1179/imtr.1985.30.1.275.

[49] M. Maurya, S. Kumar, V. Bajpai, Assessment of the mechanical properties of aluminium metal matrix composite: A review, J. Reinf. Plast. Compos. 38 (6) (2019) 267–298, https://doi.org/10.1177/0731684418816379.